
LEARNING FUNCTIONS THROUGH DIFFUSION MAPS

Alvaro Almeida Gomez
 Centro de Modelamiento Matemático
 Universidad de Chile
 Beauchef 851, Santiago, Chile
 alvaroalmeidagomez182@gmail.com

September 12, 2025

ABSTRACT

We propose a data-driven method for approximating real-valued functions on smooth manifolds, building on the Diffusion Maps framework under the manifold hypothesis. Given pointwise evaluations of a function, the method constructs a smooth extension to the ambient space by exploiting diffusion geometry and its connection to the heat equation and the Laplace-Beltrami operator.

To address the computational challenges of high-dimensional data, we introduce a dimensionality reduction strategy based on the low-rank structure of the distance matrix, revealed via singular value decomposition (SVD). In addition, we develop an online updating mechanism that enables efficient incorporation of new data, thereby improving scalability and reducing computational cost.

Numerical experiments, including applications to sparse CT reconstruction, demonstrate that the proposed methodology outperforms classical feedforward neural networks and interpolation methods in terms of both accuracy and efficiency.

Keywords Diffusion Geometry · Manifold Learning · Kernel Methods · Sparse-View CT Reconstruction

1 Introduction

Manifold learning refers to a class of nonlinear dimensionality reduction techniques aimed at uncovering the low-dimensional structure (the manifold) underlying high-dimensional data. The key assumption is that the dataset can be represented as a smooth manifold $\mathcal{M} \subset \mathbb{R}^d$. While the data are embedded in a high-dimensional ambient space, their essential variability is often confined to a much lower-dimensional smooth manifold.

The main goal of manifold learning is to reduce the dimensionality of nonlinear high-dimensional datasets while preserving their intrinsic structure. Popular approaches include t-SNE [1], kernel PCA [2], Uniform Manifold Approximation and Projection (UMAP) [3], Laplacian Eigenmaps [4], and diffusion maps [5].

Among these, diffusion maps are particularly powerful for capturing the intrinsic geometry of data. Based on the diffusion process induced by the Laplace–Beltrami operator, diffusion maps recover the true connectivity of the manifold, beyond Euclidean or geodesic distances. Unlike t-SNE or UMAP, which primarily emphasize local neighborhoods, diffusion maps reveal global connectivity and smooth transitions, making them especially suitable for time-series and dynamical systems. The method embeds the dataset into a coordinate system defined by the eigenvectors of the diffusion operator. Compared with Isomap, diffusion maps are more robust to noise and better preserve global geodesics, while providing smoother representations.

Motivated by the effectiveness of diffusion maps in capturing the intrinsic geometry of data, this paper introduces a novel data-driven methodology for approximating smooth real-valued functions

$$f : \mathcal{M} \rightarrow \mathbb{R},$$

given only a finite set of evaluations $f(x_1), f(x_2), \dots, f(x_N)$ at sampled points $\{x_i\}_{i=1}^N \subset \mathcal{M}$. The objective is to extend f to new points $x \in \mathcal{M} \setminus \{x_i\}_{i=1}^N$ in a manner that adapts to the intrinsic geometry of \mathcal{M} as revealed through the diffusion process.

The main advantage of our approach, compared to function learning methods based on neural networks such as feed-forward architectures [6,7], is that it avoids the challenges associated with training deep models. Neural networks often suffer from vanishing or exploding gradients as depth increases, which leads to unstable optimization and slow convergence [8]. In contrast, our methodology computes the approximation coefficients directly from Gaussian kernels, without the need for iterative training. This yields reduced computational cost and improved numerical stability. Furthermore, when new sample points become available, the proposed method supports online updates of the coefficients using only the new data, without recomputing the entire model.

As an application, we demonstrate the effectiveness of our approach in the sparse CT tomography problem [9, 10], where only a limited number of projections are available and the objective is to reconstruct a high-quality scan image. Traditional reconstruction methods often introduce artifacts, while recent deep learning approaches require large training datasets and strong prior knowledge of the object, which may not be available in practice. Our method, by contrast, approximates the sinogram function directly from sparse samples without any prior information, and reconstructs the image using filtered back projection. This enables reliable reconstructions in cases where deep learning methods are not feasible.

Contributions

The contributions of this paper are both theoretical and practical, and can be summarized as follows:

- We introduce a novel methodology, based on diffusion maps, for approximating smooth real-valued functions $f : \mathcal{M} \rightarrow \mathbb{R}$ from a finite number of evaluations on a manifold \mathcal{M} . The approximation exploits the intrinsic geometry of the dataset as encoded by the diffusion operator.
- We develop an efficient online update procedure that allows new sample points to be incorporated without recomputing the full approximation. This procedure relies only on local updates of the diffusion operator and kernel coefficients, thereby reducing computational complexity.
- We apply the methodology to the sparse CT tomography problem, where only a limited number of projections are available. We show that the proposed method achieves high-quality reconstructions without requiring large training datasets or prior knowledge of the object, in contrast to existing deep learning approaches.

The rest of the paper is organized as follows. In Section 2, we present the mathematical background of diffusion maps and the technical details of the proposed function approximation methodology, including the online update procedure. Section 3 discusses parameter selection to ensure numerical stability and summarizes the algorithm in Algorithm 1. Section 4 reports numerical experiments on both synthetic data and sparse CT reconstruction of clinical images. Finally, Section 5 concludes the paper and outlines directions for future research.

2 Proposed Methodology

2.1 Diffusion Maps

In this paper, we consider the Gaussian kernel G defined by

$$G(z) = \exp(-\|z\|^2). \quad (1)$$

For a fixed $\varepsilon > 0$, we introduce the rescaled Gaussian kernel G_ε as

$$G_\varepsilon(z) = G\left(\frac{z}{\varepsilon}\right) = \exp\left(-\frac{\|z\|^2}{\varepsilon^2}\right).$$

We assume the *manifold hypothesis*, which states that the dataset lies on a smooth submanifold $\mathcal{M} \subset \mathbb{R}^n$ and is distributed according to a smooth probability density function $\rho : \mathcal{M} \rightarrow \mathbb{R}$. Let $g : \mathcal{M} \rightarrow \mathbb{R}$ be a smooth function defined on the manifold \mathcal{M} . We define the convolution operator

$$\bar{g}_\varepsilon(x) = \int_{\mathcal{M}} G_\varepsilon(x - y) g(y) \rho(y) d\text{Vol}(y), \quad (2)$$

where $d\text{Vol}$ denotes the volume form induced by the Riemannian metric on \mathcal{M} . We also define the normalization function

$$d_\varepsilon(x) = \int_{\mathcal{M}} G_\varepsilon(x - y) \rho(y) d\text{Vol}(y), \quad (3)$$

and the corresponding normalized approximation

$$g_\varepsilon(x) = \frac{\bar{g}_\varepsilon(x)}{\bar{d}_\varepsilon(x)}. \quad (4)$$

The function g_ε provides a smooth approximation of g , obtained via convolution with the Gaussian kernel. This approximation is closely connected to the infinitesimal generator of the heat equation on the manifold, as established in the Diffusion Maps framework [5]. The following result, whose proof can be found in [5], formalizes this convergence and provides an asymptotic error estimate in terms of the diffusion scaling parameter ε .

Theorem 2.1. *Let $g \in C^\infty(\mathcal{M})$. Then its Gaussian approximation g_ε satisfies the infinitesimal expansion*

$$g_\varepsilon(x) = g(x) + \varepsilon \Delta g(x) + O(\varepsilon^2),$$

where Δ denotes the Laplace–Beltrami operator. In particular, g_ε converges pointwise to g as $\varepsilon \rightarrow 0$:

$$\lim_{\varepsilon \rightarrow 0} g_\varepsilon(x) = g(x), \quad \text{for all } x \in \mathcal{M}.$$

Therefore, for sufficiently small ε , g_ε serves as an effective approximation of g . Although g_ε is originally defined only on the manifold \mathcal{M} , the formulation in (2)–(4) naturally extends its definition to the ambient space \mathbb{R}^n . This extension enables the evaluation of $g_\varepsilon(x)$ for any point $x \in \mathbb{R}^n$ using only information from \mathcal{M} . In other words, based on the values of g restricted to the manifold, we can infer a smooth extension of the function to points outside \mathcal{M} .

From a computational standpoint, the Law of Large Numbers provides a foundation for approximating g_ε via Monte Carlo integration. Given a set of k i.i.d. samples $X = \{x_1, \dots, x_k\}$ drawn from the density ρ , the function $g_\varepsilon(x)$ can be approximated as

$$g_\varepsilon(x) \approx \frac{1}{\bar{d}_\varepsilon(x)} \sum_{i=1}^k G_\varepsilon(x - x_i) g(x_i), \quad (5)$$

where the empirical normalization factor is given by

$$\bar{d}_\varepsilon(x) = \sum_{i=1}^k G_\varepsilon(x - x_i).$$

Each kernel evaluation $G_\varepsilon(x - x_i)$ incurs a computational cost proportional to the ambient dimension n , resulting in an overall complexity of $\mathcal{O}(n \cdot k)$ for computing the approximation in (5). Consequently, this approach is affected by the curse of dimensionality.

To address this issue, we introduce a dimensionality reduction strategy based on low-rank projection. We assume that x lies within the hypercube $\mathcal{M} \subseteq [-M, M]^n$, and generate m i.i.d. samples

$$Z = \{z_1, z_2, \dots, z_m\}$$

from the uniform distribution over $[-M, M]^n$. Using these samples, we construct a block matrix $A_1 \in \mathbb{R}^{mk \times n}$ such that, for each $i = 1, \dots, k$, the block $A_1(i) \in \mathbb{R}^{m \times n}$ is defined as

$$A_1(i) = \begin{bmatrix} x_i - z_1 \\ x_i - z_2 \\ \vdots \\ x_i - z_m \end{bmatrix}. \quad (6)$$

The motivation for introducing the matrix A_1 is that it encodes the information of the asymmetric kernel function

$$K : \mathcal{M} \times [-M, M]^n \rightarrow \mathbb{R}^n, \quad K(x, z) = x - z,$$

which is used in the computation of the Gaussian kernel G . Such asymmetric kernels are employed to capture geometric properties and structural features of datasets, as discussed in Refs. [11–13].

We then form the full matrix A_1 by stacking these blocks, and compute its singular value decomposition (SVD):

$$A_1 = U \Sigma V^T, \quad (7)$$

where $U \in \mathbb{R}^{mk \times mk}$ and $V \in \mathbb{R}^{n \times n}$ are orthogonal matrices, and $\Sigma \in \mathbb{R}^{mk \times n}$ is a diagonal matrix whose nonzero entries are the singular values $\lambda_1 \geq \lambda_2 \geq \dots \geq \lambda_r > 0$, with $r = \text{rank}(A_1)$.

A key observation is that the singular values of A_1 reflect the average distribution of squared distances $\|x_i - z_j\|^2$ over all pairs (i, j) . In particular, the decomposition (7) yields

$$\sum_{i,j} \|x_i - z_j\|^2 = \sum_{l=1}^r \lambda_l^2,$$

demonstrating that the leading singular values encode the dominant geometric structure of X relative to Z .

To reduce dimensionality, we fix a target dimension $\bar{n} < n$ and project the dataset X onto the subspace spanned by the top \bar{n} right singular vectors $v_1, \dots, v_{\bar{n}}$. Let $\mathbf{P}_{\bar{n}}(x)$ denote the orthogonal projection of $x \in \mathbb{R}^n$ onto this subspace. We then approximate g_ε using

$$g_\varepsilon(x) \approx \frac{1}{\mathbf{Nm}_\varepsilon(x)} \sum_{i=1}^k G_\varepsilon(\mathbf{P}_{\bar{n}}(x - x_i)) g(x_i), \quad (8)$$

with normalization factor

$$\mathbf{Nm}_\varepsilon(x) = \sum_{i=1}^k G_\varepsilon(\mathbf{P}_{\bar{n}}(x - x_i)). \quad (9)$$

Since the projections $\mathbf{P}_{\bar{n}}(x_i)$ can be precomputed, the evaluation of $g_\varepsilon(x)$ at a new point $x \in [-M, M]^n \setminus \mathcal{M}$ involves two main steps: first, computing the projection $\mathbf{P}_{\bar{n}}(x)$, which has a computational cost of $\mathcal{O}(n \cdot \bar{n})$; and second, evaluating the kernel in the reduced \bar{n} -dimensional space. The latter step contributes an additional cost of $\mathcal{O}(\bar{n} \cdot k)$, yielding a total complexity of $\mathcal{O}(\bar{n}(n + k))$.

In practice, since the reduced dimension \bar{n} is typically small, this approach leads to a substantial improvement in computational efficiency. At the same time, it preserves a high level of accuracy in the approximation of g_ε , thereby offering an effective dimensionality reduction strategy for large-scale problems.

2.2 Online updating

An important advantage of the proposed algorithm is its ability to support an online updating strategy. Specifically, suppose that m new sample points $x_{k+1}, x_{k+2}, \dots, x_{k+m}$ are observed. These new samples can be incorporated into the approximation framework without requiring a full recomputation from scratch.

Given a point $x \in [-M, M]^n \setminus \mathcal{M}$, let $g_\varepsilon^{\text{prev}}(x)$ denote the approximation of $g_\varepsilon(x)$ computed using the initial set of k samples $\{x_1, x_2, \dots, x_k\}$, as defined in Equation (8). To update the estimate, we incorporate the contribution of the m newly acquired points, yielding an improved approximation $g_\varepsilon^{\text{new}}(x)$, given by:

$$g_\varepsilon^{\text{new}}(x) = \frac{1}{\mathbf{Nm}_\varepsilon^{k+m}(x)} \left[g_\varepsilon^{\text{prev}}(x) \cdot \mathbf{Nm}_\varepsilon^k(x) + \sum_{i=k+1}^{k+m} G_\varepsilon(\mathbf{P}_{\bar{n}}(x - x_i)) g(x_i) \right], \quad (10)$$

where $\mathbf{Nm}_\varepsilon^k(x)$ denotes the normalization factor associated with the initial k samples, defined similarly to Equation (9) as

$$\mathbf{Nm}_\varepsilon^k(x) = \sum_{i=1}^k G_\varepsilon(\mathbf{P}_{\bar{n}}(x - x_i)),$$

and $\mathbf{Nm}_\varepsilon^{k+m}(x)$ is the normalization factor corresponding to the full set of $k + m$ samples.

Thus, Equation (10) offers a systematic approach to update the approximation $g_\varepsilon(x)$ in an online manner, incorporating newly observed data while retaining the contributions from previously computed samples.

As an observation for further applications, if instead of having a real value function $f : [-M, M]^n \rightarrow \mathbb{R}$, we have a vector value function $f : [-M, M]^n \rightarrow \mathbb{R}^n$ a function with values \mathbb{R}^n instead of \mathbb{R} , then to its of each components

3 Numerical Stability

A crucial step in the proposed methodology is the selection of the parameter ε , which serves as an infinitesimal scale parameter in accordance with Theorem 2.1. As established therein, ε must be sufficiently small for g_ε to provide an accurate approximation of the smooth function g .

However, excessively small values of ε can lead to numerical instabilities. Specifically, the Gaussian weights

$$G_\varepsilon(z) = \exp\left(-\frac{\|z\|^2}{\varepsilon^2}\right),$$

used in the discrete approximation of Equation (8), decay rapidly as $\varepsilon \rightarrow 0$. This causes the weights to become highly concentrated near zero, thereby neglecting the influence of neighboring points and degrading the approximation quality. Moreover, the normalization factor $\mathbf{Nm}_\varepsilon(x)$, defined in Equation (9), may become extremely small, which can destabilize the reciprocal term

$$\frac{1}{\mathbf{Nm}_\varepsilon(x)}.$$

To prevent this, we choose a positive, spatially dependent parameter $\varepsilon(x)$ for all $x \in [-M, M]^n \setminus \{x_1, x_2, \dots, x_k\}$ such that the normalization factor remains uniformly bounded from below by

$$\mathbf{Nm}_{\varepsilon(x)}(x) \geq \exp(-(\log \delta)^2) > 0 \quad \text{for all } x \in [-M, M]^n \setminus \{x_1, x_2, \dots, x_k\}.$$

where $\delta > 0$ is a fixed constant. The parameter δ is called the *stabilizer parameter*. In particular, for any $\delta \in (0, 1)$ and $x \in [-M, M]^n \setminus \{x_1, x_2, \dots, x_k\}$, define

$$\varepsilon(x) = -\frac{\min_{1 \leq j \leq k} \|x - x_j\|}{\log(\delta)} > 0. \quad (11)$$

This choice guarantees that

$$\mathbf{Nm}_{\varepsilon(x)}(x) \geq \exp\left(-\left(\frac{\min_{1 \leq j \leq k} \|x - x_j\|}{\varepsilon(x)}\right)^2\right) = \exp(-(\log \delta)^2),$$

so that $\mathbf{Nm}_{\varepsilon(x)}(x)$ is uniformly bounded below by $\exp(-(\log \delta)^2)$ throughout the ambient space.

This construction is robust under online updates. Suppose that, for a given $x \in [-M, M]^n \setminus \{x_1, x_2, \dots, x_k\}$, $\varepsilon(x)$ is chosen from an initial set of k samples as

$$\varepsilon(x) = -\frac{\min_{1 \leq j \leq k} \|x - x_j\|}{\log(\delta)}. \quad (12)$$

After adding m new samples to the dataset (as in Equation (10)), we still have

$$\mathbf{Nm}_{\varepsilon(x)}^{k+m}(x) \geq \exp\left(-\left(\frac{\min_{1 \leq j \leq k} \|x - x_j\|}{\varepsilon(x)}\right)^2\right) = \exp(-(\log \delta)^2),$$

Hence, the previously chosen $\varepsilon(x)$ remains valid after the update, ensuring stability of the denominator $\mathbf{Nm}_\varepsilon(x)$ throughout the entire updating process.

Finally, we remark that the parameter $\varepsilon(x)$ is chosen only for points $x \neq x_i$ with $1 \leq i \leq n$, since our goal is to compute the approximation $g_\varepsilon(x)$ at points outside the training set. For the training points x_i , this computation is unnecessary because the values $g(x_i)$ are already known.

We summarize the proposed methodology, including the selection of the parameter ε , in Algorithm 1.

Algorithm 1 Learning functions through Diffusion Maps

Input:

- Data set $X = \{x_1, x_2, \dots, x_N\}$,
- Function evaluations $g(x_1), g(x_2), \dots, g(x_N)$,
- Target dimension \bar{n} for dimensionality reduction,
- Number of training points m sampled uniformly from the cube $[-M, M]^n$,
- Stabilizer parameter $0 < \delta < 1$,
- Query point $x \in [-M, M]^n \setminus \{x_1, x_2, \dots, x_N\}$.

Procedure:

1. Generate m i.i.d. sample points from the uniform distribution on the n -dimensional cube $[-M, M]^n$.
2. Construct the matrix A_1 as defined in Eq. (6).
3. Compute the singular value decomposition of A_1 (Eq. (7)).
4. Define $\mathbf{P}_{\bar{n}}$ as the orthogonal projection onto the subspace spanned by the top \bar{n} right singular vectors of A_1 .
5. Compute the parameter ε according to Eq. (12).
6. Evaluate the approximation $g_\varepsilon(x)$ using Eq. (8).

Output: Approximation $g_\varepsilon(x)$ of $g(x)$.

4 Applications and Computational Experiments

In this section, we present two numerical experiments to validate and illustrate the proposed methodology.

The first experiment is a synthetic example based on a logarithmic spiral curve. Its purpose is to evaluate how the methodology captures geometric patterns from the latent manifold, how it can be used to extrapolate function values outside the manifold, and how accurately it approximates function values at additional points distributed along the same manifold.

The second experiment concerns the sparse CT tomography problem, where only a limited number of projections are available and the goal is to reconstruct high-quality images. This is an ill-posed inverse problem. Our approach interpolates the sinogram using the proposed methodology, followed by image reconstruction via filtered back-projection.

In both experiments, we compare the proposed methodology against a feedforward neural network. Beyond reporting numerical results, we highlight how the proposed method more effectively extracts geometric patterns from the training data than the neural network.

Although the methodology is designed for high-dimensional data, the following experiments are carried out in a two-dimensional setting to provide clearer visualizations of the results. Nevertheless, the framework is intended to extend to higher-dimensional spaces.

All experiments employ Algorithm 1 with target dimension $\bar{n} = 2$ and stabilizer parameter $\delta = 0.1$. The numerical implementation was performed in MATLAB on a laptop equipped with an Intel Core i5-1235U 1.30 GHz processor and 8 GB of RAM.

4.1 Synthetic Experiment

To illustrate how the proposed method works, we consider the logarithmic spiral curve, which is a one-dimensional smooth manifold. The curve is parametrized by $\alpha : [0, 1] \rightarrow \mathbb{R}^2$ in Cartesian coordinates as

$$\alpha(t) = e^t (\cos(2\pi t), \sin(2\pi t)).$$

We denote this logarithmic spiral curve by \mathcal{M} . Next, we define a real-valued function $f : \mathcal{M} \rightarrow \mathbb{R}$ by

$$f(x) = \log(\|x\|), \tag{13}$$

where $\|\cdot\|$ denotes the Euclidean norm. Observe that this function is the inverse of the parametrization α , in the sense that

$$f(\alpha(t)) = t, \quad \text{for all } t \in [0, 1].$$

The spiral curve \mathcal{M} and the logarithmic function defined in Eq. (13) are shown in Figure 1.

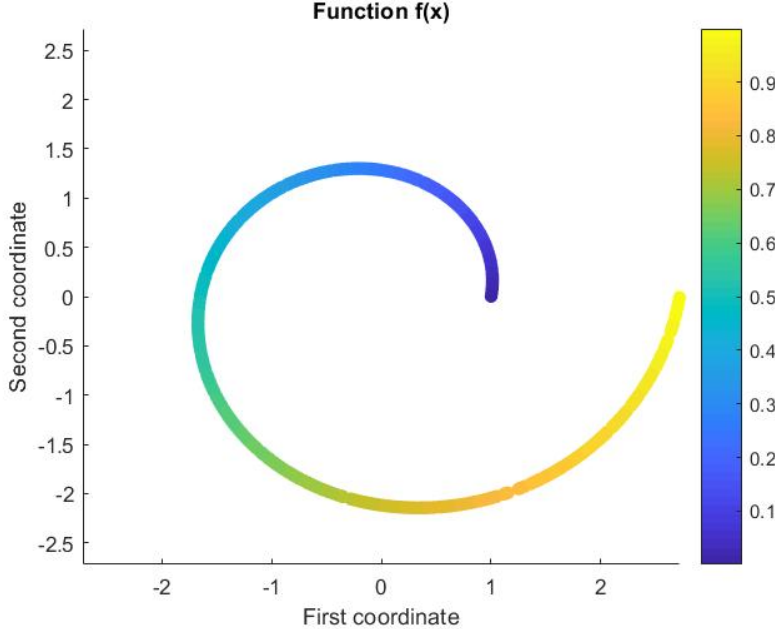


Figure 1: The logarithmic spiral curve \mathcal{M} and the logarithmic function $f(x)$ defined in Eq. (13).

The purpose of this experiment is twofold. First, we investigate how well the method can learn the function outside the logarithmic spiral curve, i.e., over the two-dimensional cube $[-\exp(1), \exp(1)]^2$, and what kinds of patterns the learning procedure can extract from the dataset. Second, we study how accurately the method can recover the logarithmic function f along the spiral curve \mathcal{M} .

For both objectives, we generate several sample sets over the logarithmic spiral curve \mathcal{M} . Specifically, we consider 50, 100, and 150 sample points drawn uniformly along the manifold, together with 10^4 points drawn uniformly from the cube $[-\exp(1), \exp(1)]^2$. For the first objective, we analyze the types of patterns that the learning procedure can extract from this dataset. For the second objective, we quantitatively evaluate how well the method approximates the logarithmic function defined in Eq. (13). In both cases, we compare the proposed method with a feedforward neural network consisting of 10 hidden layers, trained via gradient descent. The numerical implementation, written in MATLAB, is available in the GitHub repository [14].

In Figure 2, we illustrate the learning procedure over the two-dimensional cube $[-e^1, e^1]^2$. The target function f , defined in Eq. (13), is originally specified only on the logarithmic spiral curve \mathcal{M} and then extended to the entire domain $[-\exp(1), \exp(1)]^2$. Figure 3 shows the learning of f using increasing numbers of sample points distributed along \mathcal{M} .

From Figure 2, we observe that the proposed methodology successfully reproduces the spiral pattern throughout the cube $[-\exp(1), \exp(1)]^2$, consistent with the structure of \mathcal{M} , while the feed-forward neural network fails to capture this global pattern. Table 1 provides a quantitative evaluation of the learning procedure shown in Figure 3, reporting the squared error defined as the Frobenius norm between the exact values of f and the learned approximations. The results indicate that, regardless of the number of training points (batch size), the proposed method achieves consistently smaller errors than the feed-forward neural network. This superiority is also evident in Figure 3, where the proposed approach accurately captures the spiral pattern along \mathcal{M} , in contrast to the neural network, which fails to reproduce it.

Batch size	Proposed Methodology	FNN
50	1.46	2925.09
100	0.61	2920.28
150	0.40	3230.45

Table 1: Squared error, defined as the Frobenius norm between the exact values of f in Eq. (13) and the learned approximations, computed for different sample sizes (batch sizes) using the proposed methodology and the feed-forward neural network (FNN).

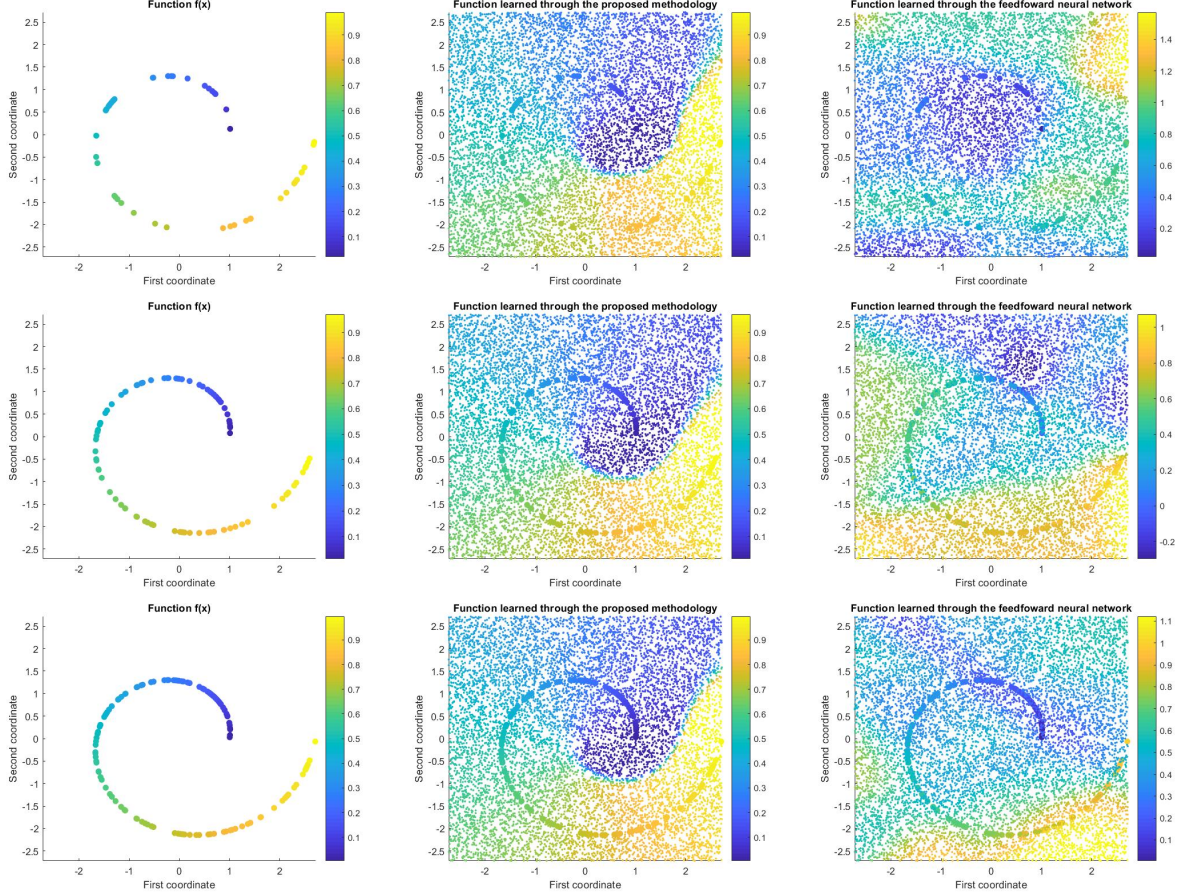


Figure 2: The first column (left) shows the dataset, the middle column displays the learned function f defined in Eq. (13) and obtained with the proposed methodology over the two-dimensional cube $[-\exp(1), \exp(1)]^2$, and the right column shows the learned function obtained with a feed-forward neural network. From top to bottom, the rows correspond to 50, 100, and 150 sample points on the logarithmic spiral curve, respectively.

4.2 Sparse-View Tomographic Reconstruction

In sparse-view computed tomography (CT), the objective is to reconstruct high-quality tomographic images from a substantially reduced number of projection samples, Ref. [15, 16]. A primary clinical motivation for sparse-view CT is the reduction of radiation dose, thereby mitigating potential health risks for patients. In addition, the decreased number of projections shortens scan time, improving patient comfort.

Sparse-view CT poses significant challenges due to the limited availability of projection data, which leads to an ill-posed inverse problem. Classical analytical reconstruction methods, such as filtered back projection (FBP), perform poorly under these conditions. Iterative reconstruction methods can provide improved image quality; however, their performance deteriorates under severe undersampling, particularly in the absence of reliable *a priori* information. In addition, these methods typically incur substantial computational costs.

In recent years, deep learning approaches have been proposed to address sparse-view reconstruction [10, 17–19]. While these methods have shown promising results, they typically rely on strong data-driven priors and require representative *a priori* image information, which may not be available when reconstructing tomographic objects with unknown structural characteristics.

In this work, we propose a framework to synthetically augment sparse projection data by generating additional projection views directly in the sinogram domain. The key idea is to enrich the sampled angular space by exploiting the underlying geometric structure of the projection directions. Specifically, we model the set of projection angles as a smooth one-dimensional submanifold, namely the circle S^1 . By learning on this manifold, we aim to generate

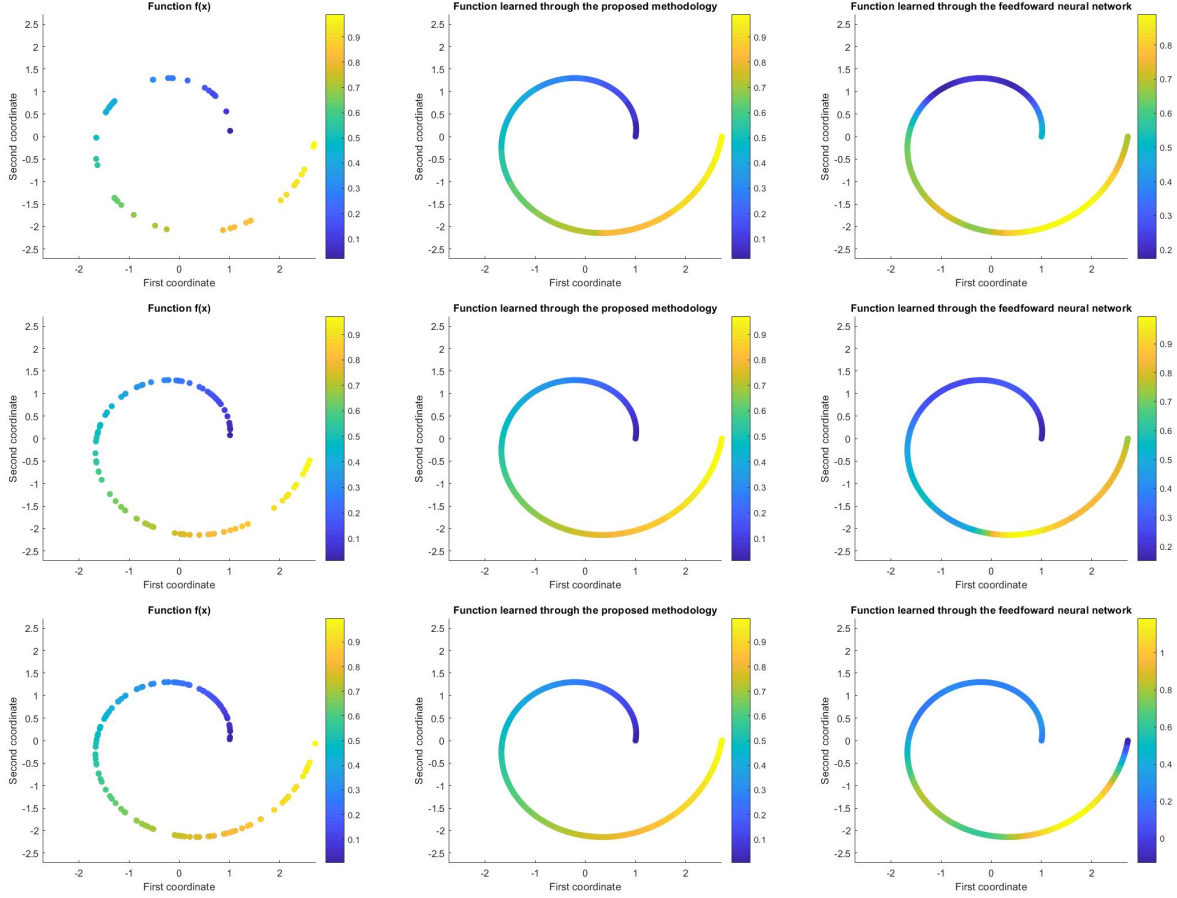


Figure 3: The first column (left) shows the dataset, the middle column displays the learned function f defined in Eq. (13) and obtained with the proposed methodology over the logarithmic spiral curve \mathcal{M} , and the right column shows the learned function obtained with a feed-forward neural network. From top to bottom, the rows correspond to 50, 100, and 150 sample points on \mathcal{M} , respectively.

consistent synthetic projections at new angular positions, thereby improving reconstruction quality from sparse-view data using FBP.

A notable advantage of the proposed methodology over deep learning approaches is that it does not require *a priori* image information. Instead, it leverages the intrinsic geometric structure of the projection space.

The proposed procedure consists of two main steps:

1. Generate additional tomographic projections at new angular positions using the proposed method.
2. Apply FBP to the augmented dataset to obtain higher-quality reconstructions.

We evaluate the proposed methodology on three different images: the Shepp–Logan phantom, a human head, and a human abdomen. The human images were taken from the public dataset of the National Library of Medicine, as reported in Ref. [20]. These three images are shown in Fig. 4.

In the following experiments, we use the parameter settings described below. The methodology is tested with batch sizes 50, 100, and 150, corresponding to sparse angular positions uniformly distributed in $[0, 180]$, where the tomographic projections are taken. We refer to this set of projections as the *training dataset*.

An additional batch of 10^4 angles is randomly generated from the uniform distribution on $[0, 180]$. We refer to this set of projections as the *learned dataset*. The stabilizer parameter δ , used to compute the infinitesimal parameters $\varepsilon(x)$ as defined in Eq. 11, is fixed at $\delta = 1$.

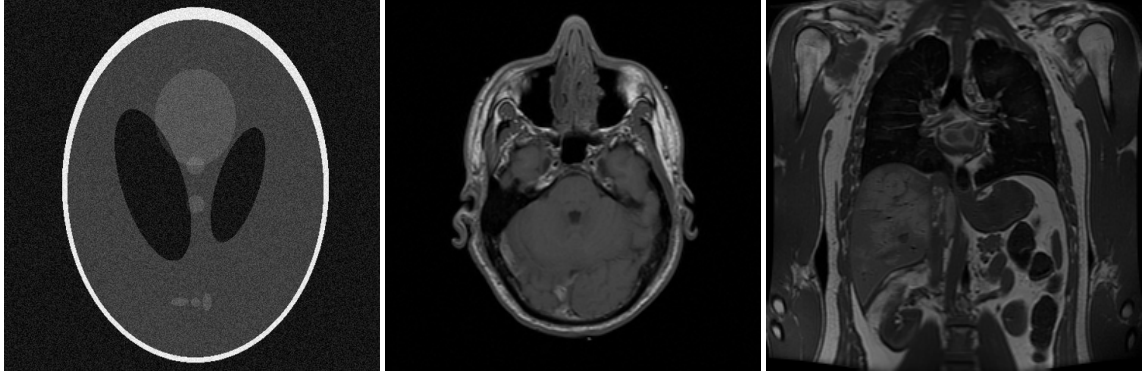


Figure 4: From left to right: Shepp-Logan phantom, human head, and human abdomen. The human images were taken from [20].

In the proposed model, the reconstruction is studied under additive noise of magnitude 20%. Let X denote the image to be reconstructed, represented as a $d \times d$ array. The noisy observation is then defined as

$$X_{\text{noisy}} = X + 0.2 \times Z,$$

where Z is a $d \times d$ matrix with independent entries uniformly distributed on $[0, 1]$.

We compare the proposed methodology with a feed-forward neural network trained via gradient descent and with cubic spline interpolation. The neural network has 10 hidden layers, taking the projection angle as input and producing the corresponding projection as output. Training is performed on the *training dataset*, and inference on the *learned dataset* generates sinograms from both the neural network and the cubic spline interpolation. These sinograms are then used to reconstruct the tomographic image with the Filtered Back Projection (FBP) algorithm. All numerical implementations were written in MATLAB, and the code is available in the GitHub repository [21].

In Figures 5, 7, and 9, we present the sinograms, and in Figures 6, 8, and 10 the corresponding tomographic reconstructions of the Shepp-Logan phantom, a human head, and a human abdomen, respectively. Each figure shows results obtained from: (i) sparse projections using only the training samples, (ii) interpolation of the projections with the proposed methodology, (iii) interpolation of the projections with a feed-forward neural network, and (iv) interpolation of the projections with cubic spline interpolation. Columns (left to right) correspond to cases (i)–(iv), while rows (top to bottom) correspond to reconstructions obtained with 50, 100, and 150 training samples, respectively.

In addition, Tables 2, 3, and 4 report the squared error, computed as the Frobenius norm of the difference between the original image and the reconstructed approximations. This error provides a quantitative measure of the reconstruction quality for the Shepp-Logan phantom, the human head, and the human abdomen. The results show that the *Learned* column, corresponding to the proposed methodology, consistently achieves a lower mean squared error (MSE) than the reconstructions obtained from sparse training data, the feed-forward neural network (FNN), and cubic spline interpolation. This confirms that the proposed methodology outperforms the other approaches. The visual comparisons in Figures 6, 8, and 10 further support this conclusion, as the reconstructions in the middle column (proposed method) exhibit higher visual quality. Overall, these results demonstrate the superior performance of the proposed methodology in tomographic image reconstruction, without requiring any *a priori* knowledge of the sparse dataset.

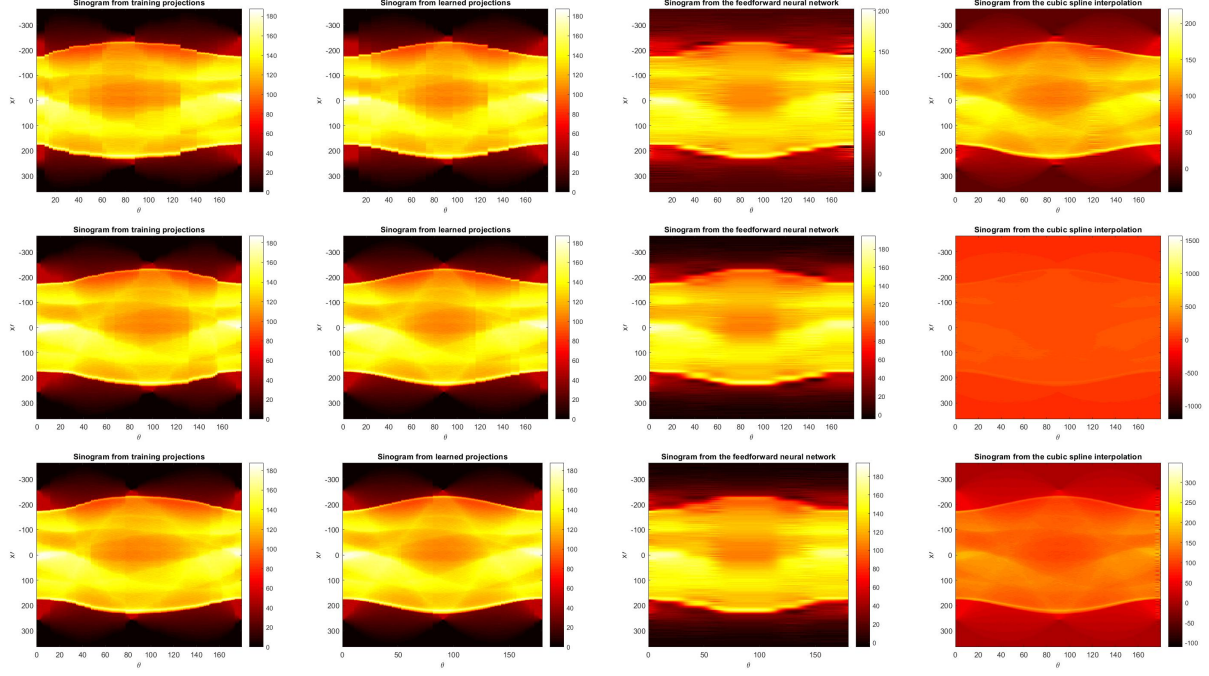


Figure 5: Sinograms of tomographic projections of the Shepp-Logan phantom. Columns (left to right): (i) sparse projections from the learning set, (ii) interpolation obtained with the proposed methodology, (iii) interpolation obtained from a feedforward neural network. (iv) interpolation of the projections with cubic spline Rows (top to bottom): results using 50, 100, and 150 training samples, respectively.

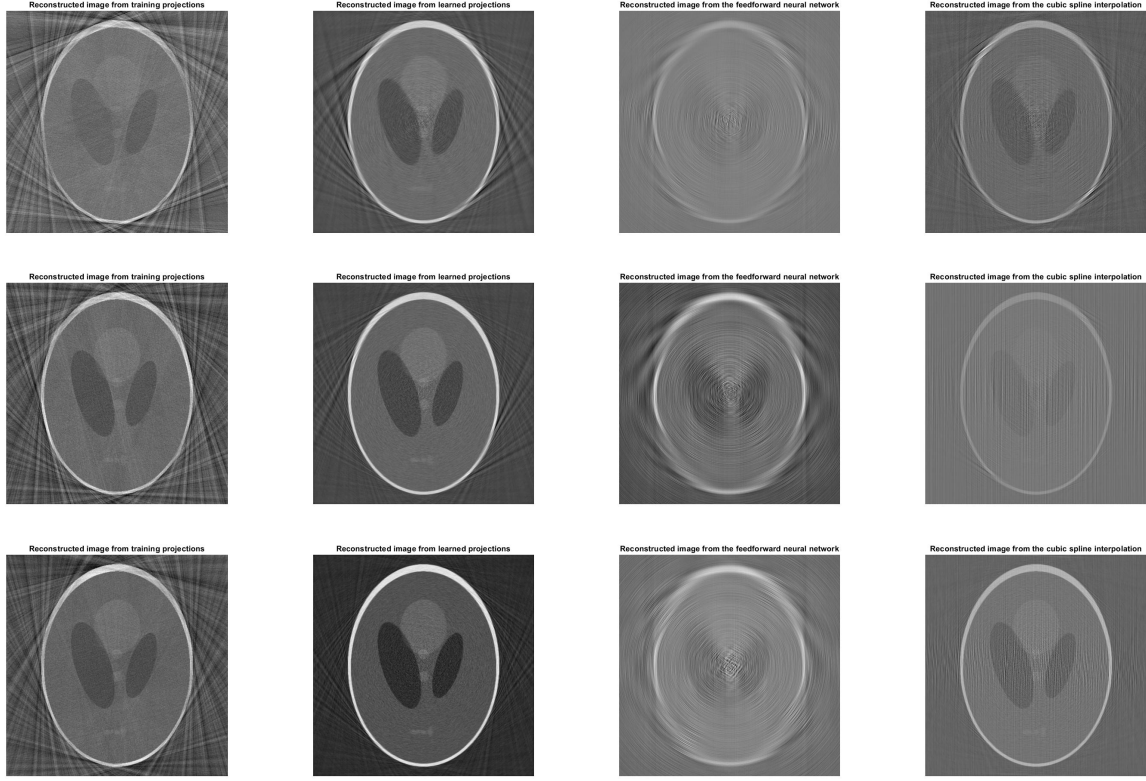


Figure 6: Tomographic reconstruction of the Shepp–Logan phantom. Columns (left to right): (i) sparse projections from the learning set, (ii) interpolation obtained with the proposed methodology, (iii) interpolation obtained from a feedforward neural network. (iv) interpolation of the projections with cubic spline Rows (top to bottom): results using 50, 100, and 150 training samples, respectively.

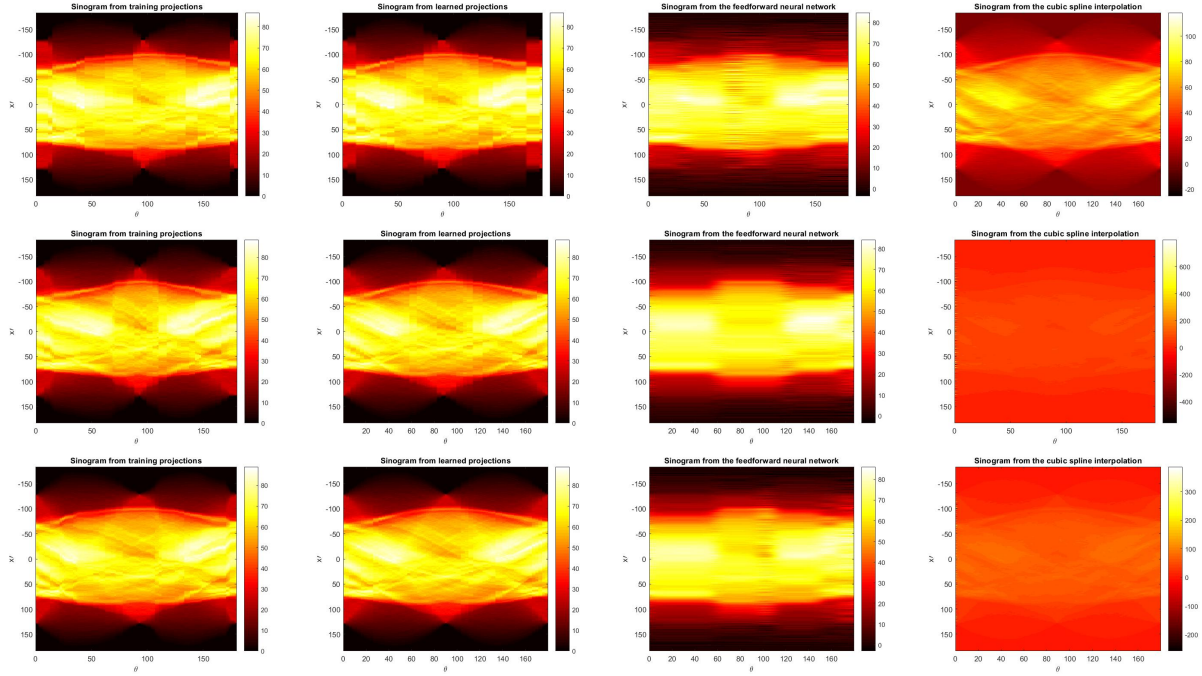


Figure 7: Sinograms of tomographic projections of a human head. Columns (left to right): (i) sparse projections from the learning set, (ii) interpolation obtained with the proposed methodology, (iii) interpolation obtained from a feedforward neural network. (iv) interpolation of the projections with cubic spline. Rows (top to bottom): results using 50, 100, and 150 training samples, respectively.

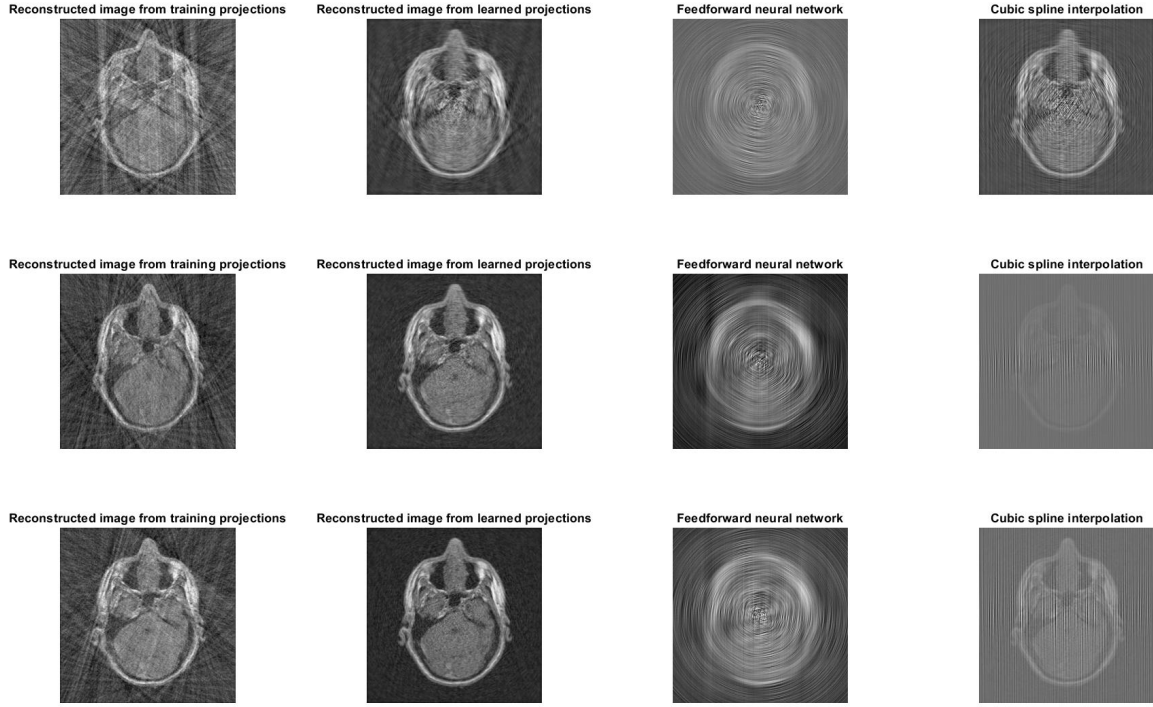


Figure 8: Tomographic reconstruction of a human head. Columns (left to right): (i) sparse projections from the learning set, (ii) interpolation obtained with the proposed methodology, (iii) interpolation obtained from a feedforward neural network. (iv) interpolation of the projections with cubic spline Rows (top to bottom): results using 50, 100, and 150 training samples, respectively.

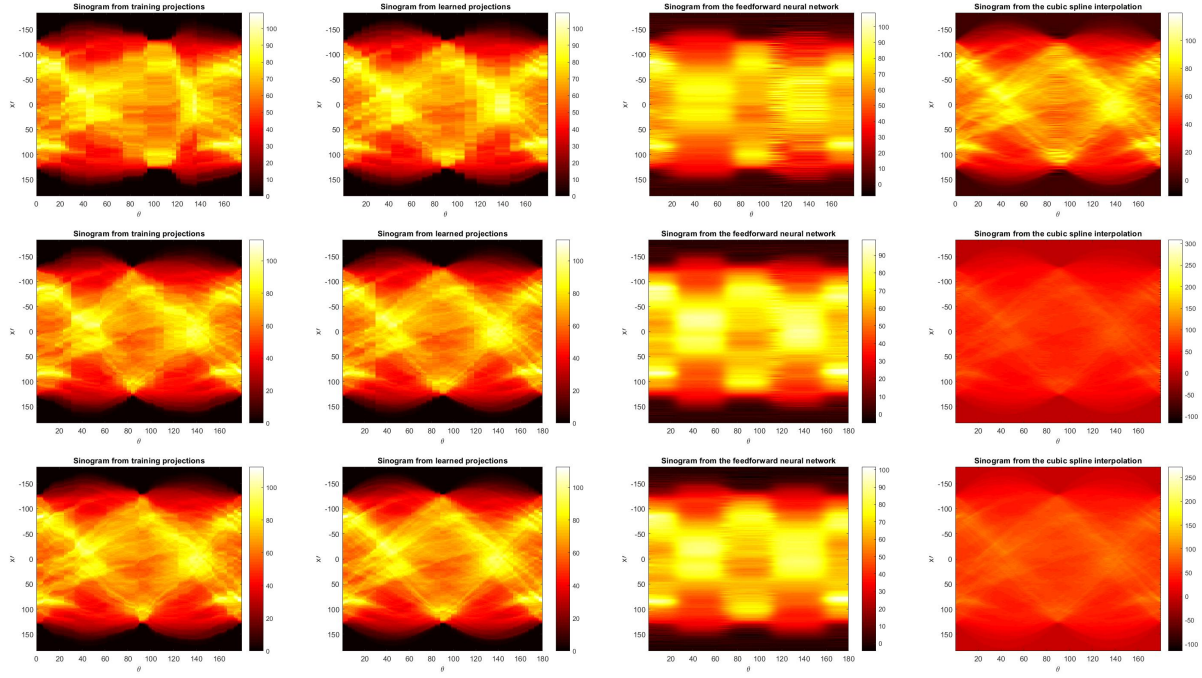


Figure 9: Sinograms of tomographic projections of a human abdomen. Columns (left to right): (i) sparse projections from the learning set, (ii) interpolation obtained with the proposed methodology, (iii) interpolation obtained from a feedforward neural network. (iv) interpolation of the projections with cubic spline Rows (top to bottom): results using 50, 100, and 150 training samples, respectively.

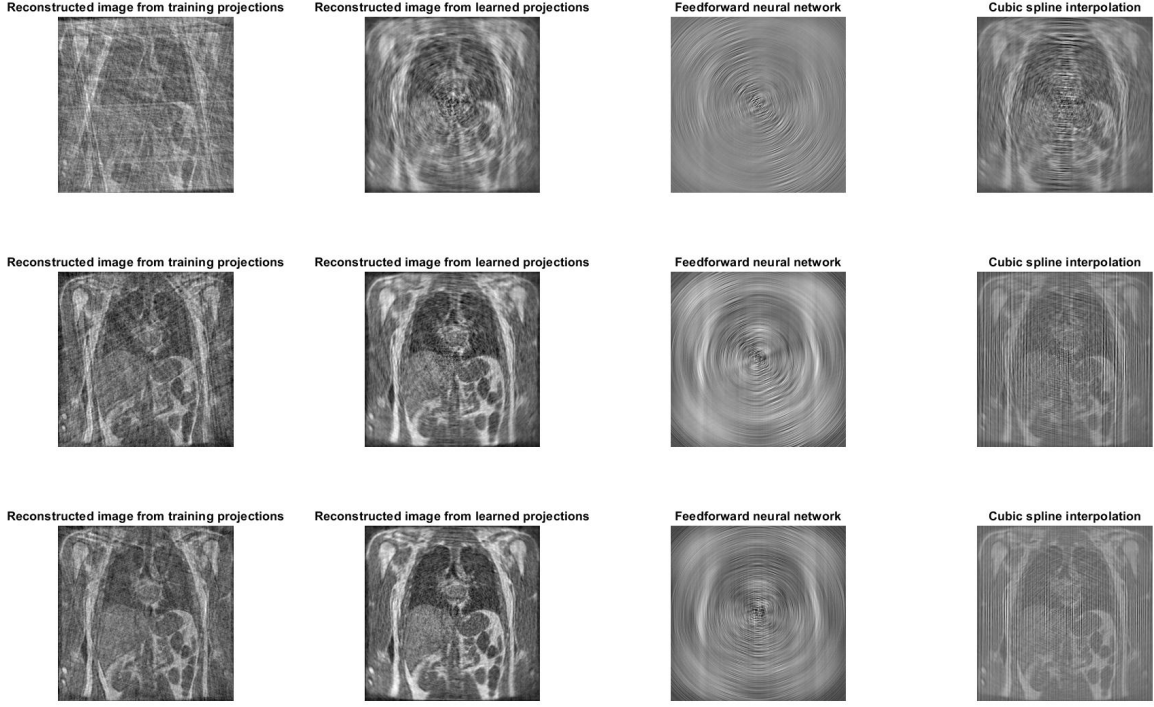


Figure 10: Tomographic reconstruction of a human abdomen. Columns (left to right): (i) sparse projections from the learning set, (ii) interpolation obtained with the proposed methodology, (iii) interpolation obtained from a feedforward neural network. (iv) interpolation of the projections with cubic spline Rows (top to bottom): results using 50, 100, and 150 training samples, respectively.

Batch size	Training	Learned	FNN	Spline
50	95.69	39.84	107.95	63.79
100	68.62	26.70	73.87	281.18
150	55.82	20.34	75.23	79.72

Table 2: Squared error for the Shepp–Logan phantom reconstruction. The *Training* column reports the error obtained using only the sparse training dataset, the *Learned* column shows the results of the proposed methodology, the *FNN* column reports the error obtained with the feed-forward neural network, and the *Spline* column gives the error from cubic spline interpolation.

Batch size	Training	Learned	FNN	Spline
50	26.22	14.43	34.48	20.13
100	18.50	8.24	25.20	175.00
150	14.94	6.82	27.23	71.15

Table 3: Squared error for the human head reconstruction. The *Training* column reports the error obtained using only the sparse training dataset, the *Learned* column shows the results of the proposed methodology, the *FNN* column reports the error obtained with the feed-forward neural network, and the *Spline* column gives the error from cubic spline interpolation.

Batch size	Training	Learned	FNN	Spline
50	29.87	17.23	40.52	23.13
100	18.36	11.23	25.17	35.35
150	14.95	8.49	25.60	34.33

Table 4: Squared error for the human abdomen reconstruction. The *Training* column reports the error obtained using only the sparse training dataset, the *Learned* column shows the results of the proposed methodology, the *FNN* column reports the error obtained with the feed-forward neural network, and the *Spline* column gives the error from cubic spline interpolation.

5 Conclusion and Future Work

In this paper, we proposed a novel data-driven approach for approximating smooth functions defined over manifolds. A central contribution is the computation of the scale-time diffusion parameter ε in a manner that preserves the computational stability of the method. Furthermore, the approach incorporates an online updating mechanism, which results in faster training compared to traditional neural networks. We also demonstrated the applicability of the method to sparse CT reconstruction problems.

The numerical experiments show that the proposed methodology achieves superior performance relative to other data-driven approximation techniques, including feedforward neural networks. Building on these promising results, future work will focus on extending the methodology to engineering and financial applications, where neural networks are commonly employed to approximate complex target functions. In particular, we aim to explore its integration with reinforcement learning techniques for solving large-scale dynamic problems in the financial industry [22–24], as well as in mechanical engineering, where neural networks have been widely applied to the numerical solution of large-scale partial differential equations [25–27].

Acknowledgements. The author was supported by Centro de Modelamiento Matemático (CMM) BASAL fund FB210005 for center of excellence from ANID-Chile. The author also gratefully acknowledges the participants of the Postdoctoral Seminar for their valuable suggestions and insightful comments that contributed to improving this manuscript.

References

- [1] T Tony Cai and Rong Ma. Theoretical foundations of t-sne for visualizing high-dimensional clustered data. *Journal of Machine Learning Research*, 23(301):1–54, 2022.
- [2] Bernhard Schölkopf, Alexander Smola, and Klaus-Robert Müller. Kernel principal component analysis. In *International conference on artificial neural networks*, pages 583–588. Springer, 1997.
- [3] Leland McInnes, John Healy, and James Melville. Umap: Uniform manifold approximation and projection for dimension reduction. *arXiv preprint arXiv:1802.03426*, 2018.
- [4] Mikhail Belkin and Partha Niyogi. Laplacian eigenmaps for dimensionality reduction and data representation. *Neural computation*, 15(6):1373–1396, 2003.
- [5] Ronald R Coifman and Stéphane Lafon. Diffusion maps. *Applied and computational harmonic analysis*, 21(1):5–30, 2006.
- [6] Daniel Svozil, Vladimir Kvasnicka, and Jiri Pospichal. Introduction to multi-layer feed-forward neural networks. *Chemometrics and intelligent laboratory systems*, 39(1):43–62, 1997.
- [7] George Bebis and Michael Georgopoulos. Feed-forward neural networks. *Ieee Potentials*, 13(4):27–31, 2002.
- [8] Xavier Glorot and Yoshua Bengio. Understanding the difficulty of training deep feedforward neural networks. In *Proceedings of the thirteenth international conference on artificial intelligence and statistics*, pages 249–256. JMLR Workshop and Conference Proceedings, 2010.
- [9] Zhicheng Zhang, Xiaokun Liang, Xu Dong, Yaoqin Xie, and Guohua Cao. A sparse-view ct reconstruction method based on combination of densenet and deconvolution. *IEEE transactions on medical imaging*, 37(6):1407–1417, 2018.

- [10] Peng Bao, Wenjun Xia, Kang Yang, Jiliu Zhou, and Yi Zhang. Sparse-view ct reconstruction via convolutional sparse coding. In *2019 IEEE 16th International Symposium on Biomedical Imaging (ISBI 2019)*, pages 1446–1449. IEEE, 2019.
- [11] Alvaro Almeida Gomez, Antônio J Silva Neto, and Jorge P Zubelli. Diffusion representation for asymmetric kernels. *Applied Numerical Mathematics*, 166:208–226, 2021.
- [12] Mingzhen He, Fan He, Ruikai Yang, and Xiaolin Huang. Diffusion representation for asymmetric kernels via magnetic transform. *Advances in Neural Information Processing Systems*, 36:53742–53761, 2023.
- [13] Alvaro Almeida Gomez, Antônio J Silva Neto, and Jorge P Zubelli. A diffusion-map-based algorithm for gradient computation on manifolds and applications. *IEEE Access*, 11:90622–90640, 2023.
- [14] Alvaro Almeida Gomez. Numerical implementation of learning functions through diffusion maps in MATLAB. <https://github.com/alvaroalmeidagomez/LTD/tree/main/SE>, 2025. Accessed: September 2, 2025.
- [15] Jing Huang, Yunwan Zhang, Jianhua Ma, Dong Zeng, Zhaoying Bian, Shanzhou Niu, Qianjin Feng, Zhengrong Liang, and Wufan Chen. Iterative image reconstruction for sparse-view ct using normal-dose image induced total variation prior. *PloS one*, 8(11):e79709, 2013.
- [16] Sajid Abbas, Jonghwan Min, and Seungryong Cho. Super-sparsely view-sampled cone-beam ct by incorporating prior data. *Journal of X-ray science and technology*, 21(1):71–83, 2013.
- [17] Hu Chen, Yi Zhang, Yunjin Chen, Junfeng Zhang, Weihua Zhang, Huaiqiang Sun, Yang Lv, Peixi Liao, Jiliu Zhou, and Ge Wang. Learn: Learned experts’ assessment-based reconstruction network for sparse-data ct. *IEEE transactions on medical imaging*, 37(6):1333–1347, 2018.
- [18] Hoyeon Lee, Jongha Lee, Hyeongseok Kim, Byungchul Cho, and Seungryong Cho. Deep-neural-network-based sinogram synthesis for sparse-view ct image reconstruction. *IEEE Transactions on Radiation and Plasma Medical Sciences*, 3(2):109–119, 2018.
- [19] Jia Wu, Jinzhao Lin, Xiaoming Jiang, Wei Zheng, Lisha Zhong, Yu Pang, Hongying Meng, and Zhangyong Li. Dual-domain deep prior guided sparse-view ct reconstruction with multi-scale fusion attention. *Scientific Reports*, 15(1):16894, 2025.
- [20] National Library of Medicine NLM. he visible human project. <https://www.nlm.nih.gov/research/visible/mri.html>, 2025. Accessed: September 2, 2025.
- [21] Alvaro Almeida Gomez. Numerical implementation of sparse ct reconstruction in MATLAB. https://github.com/alvaroalmeidagomez/LTD/tree/main/Sparse_CT, 2025. Accessed: September 2, 2025.
- [22] Giorgio Consigli, Alvaro A Gomez, and Jorge P Zubelli. Optimal dynamic fixed-mix portfolios based on reinforcement learning with second order stochastic dominance. *Engineering Applications of Artificial Intelligence*, 133:108599, 2024.
- [23] Anthony Coache and Sebastian Jaimungal. Reinforcement learning with dynamic convex risk measures. *Mathematical Finance*, 34(2):557–587, 2024.
- [24] Álvaro Cartea, Sebastian Jaimungal, and Leandro Sánchez-Betancourt. Reinforcement learning for algorithmic trading. *Machine Learning and Data Sciences for Financial Markets: A Guide to Contemporary Practices*. Cambridge University Press, 2023.
- [25] Justin Sirignano and Konstantinos Spiliopoulos. Dgm: A deep learning algorithm for solving partial differential equations. *Journal of computational physics*, 375:1339–1364, 2018.
- [26] Jiequn Han, Arnulf Jentzen, and Weinan E. Solving high-dimensional partial differential equations using deep learning. *Proceedings of the National Academy of Sciences*, 115(34):8505–8510, 2018.
- [27] Lu Lu, Xuhui Meng, Zhiping Mao, and George Em Karniadakis. Deepxde: A deep learning library for solving differential equations. *SIAM review*, 63(1):208–228, 2021.